Evaluating Piezoelectric Materials for Power Conversion

Jessica D. Boles*, Pedro L. Acosta*, Yogesh K. Ramadass†, Jeffrey H. Lang* and David J. Perreault*
*Massachusetts Institute of Technology, Cambridge, MA, USA
†Texas Instruments, Santa Clara, CA, USA
Email: jboles@mit.edu

***Abstract*—Piezoelectric energy storage has several potential advantages for use in power conversion; it offers very high power density and efficiency capabilities, especially compared to magnetics at small scales. Converter architectures have been developed for efficient utilization of piezoelectrics, but without fundamental criteria for selecting the piezoelectric devices themselves. In this paper, we derive figures of merit for piezoelectric materials in power electronics based on achievable efficiency and power density, assuming realistic converter operation. We then apply these metrics to evaluate 51 commercially-available PZT piezoelectric materials and identify promising candidates. These figures of merit and their associated geometry conditions serve as guidelines for high-efficiency, high-power density piezoelectric resonator design, which we demonstrate and validate in LTSpice. With both mechanical efficiency and physical limits constrained, it is shown that piezoelectrics demonstrate favorable scaling properties for miniaturized power conversion.**

I. Introduction

Magnetic energy storage poses a fundamental limit to miniaturization for power electronics [1], [2]. This motivates exploration of power conversion based on other energy storage technologies such as piezoelectrics, which have very high power density and efficiency capabilities with improved scaling properties to small sizes [3]. Piezoelectrics store energy in the mechanical compliance and inertia of a piezoelectric material and can be realized as single-port piezoelectric resonators (PRs) or multi-port piezoelectric transformers (PTs). Piezoelectrics also offer other advantages such as planar form factors, ease of batch fabrication, and the potential to use the energy storage element itself for electrical isolation (with PTs).

The promise of power conversion based on only piezoelectric energy storage is evident in magnetic-less converter designs realized in [4]–[7] with PRs and [8]–[12] with PTs. [4] enumerates practical converter implementations that achieve high efficiency through optimal utilization of the PR across the switching cycle, resulting in experimental efficiencies exceeding 99%. However, criteria for selecting piezoelectric materials and/or designing PRs themselves remain murky in the context of power conversion, and metrics developed for other applications serve different interests.

This material is based upon work supported by Texas Instruments, the National Science Foundation Graduate Research Fellowship Program under Grant No. 1122374, and the Cooperative Agreement between the Masdar Institute of Science and Technology (Masdar Institute), Abu Dhabi, UAE and the Massachusetts Institute of Technology (MIT), Cambridge, MA, USA - Reference 02/MI/MIT/CP/11/07633/GEN/G/00.

TABLE I
State and Parameter Definitions

δ	Mech. Displacement (m)
T	Mech. Stress (N/m^2)
S	Mech. Strain
E	Elec. Field Strength (N/m)
D	Elec. Flux Density (C/m^2)
Y	Young's Modulus (N/m^2)
d	Piezoelectric Constant (C/N)
ϵ	Dielectric Constant (F/m)
ρ	Density (kg/m^3)
k	Electromechanical Coupling Factor

In this work, we present evaluation metrics for piezoelectric materials specifically for use as energy storage components in power electronics. In particular, we focus on figures of merit (FOMs) based on minimum mechanical loss ratio and maximum power density, which can be derived for a realistic converter control sequence to be functions of only material properties. We demonstrate the use of both FOMs to evaluate and identify promising piezoelectric materials, which we then utilize in an example design to validate these analyses in LTspice. In addition to material selection, these FOM derivations aid PR geometry design and elucidate the fundamental power handling scaling properties for a PR in a realistic converter implementation.

II. Piezoelectric Resonator Model

Deriving metrics for piezoelectric materials first requires appropriate models for the PR's mechanical and electrical behaviors in a converter. To begin, we assume the PR illustrated in Fig. 1(a), which has electrode area A and distance l between electrodes, with one electrode solidly mounted on a conductive surface. For excitation of its thickness extensional vibration mode (ie. the elastic wave propagates parallel to the electric field, both along the z axis), this PR's behavior is governed by the following coupled state equations and Newtonian mechanics equation, respectively [13], [14]:

$$\frac{\partial \delta_3}{\partial z} = \frac{1}{Y_{33}^E} T_3 + d_{33} E_3 \tag{1}$$

$$D_3 = d_{33} T_3 + \epsilon_3^T E_3 \tag{2}$$

$$\rho \frac{\partial^2 \delta_3}{\partial t^2} = \frac{\partial T_3}{\partial z} \tag{3}$$

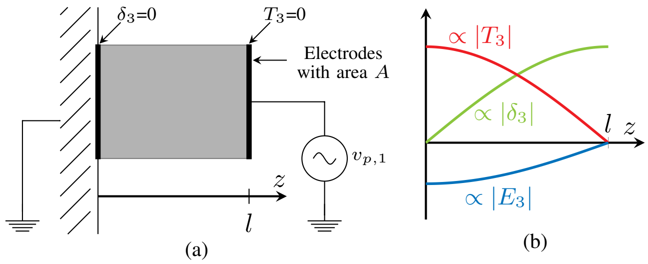

Fig. 1. (a) Side view of a solidly-mounted PR in thickness vibration mode. (b) Relative magnitudes of δ_3, T_3, and E_3 as functions of z for this PR.

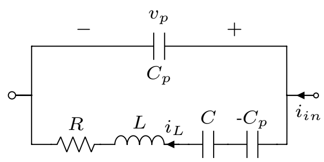

Fig. 2. Butterworth-Van Dyke circuit model for PRs in thickness extensional vibration mode [13], [15].

Parameters for these equations are defined in Table I; superscripts indicate constant conditions for measurement, and subscripted 3's indicate the polarization direction (z-direction in this case). Together, (1)-(3) constitute the following wave equation for mechanical displacement δ_3:

$$\rho\left(1-\frac{d_{33}^2 Y_{33}^E}{\epsilon_3^T}\right)\frac{\partial^2\delta_3}{\partial t^2}=Y_{33}^E\frac{\partial^2\delta_3}{\partial z^2} \tag{4}$$

Assuming the lowest resonant mode for the boundary conditions in Fig. 1(a), the wave equation of (4) dictates the z-dependent amplitudes for δ_3, E_3, and T_3 shown in Fig. 1(b). They have the following analytical expressions[1], where Δ is the maximum δ, κ is the wave number (in rad/m), and $k_{33}^2=\frac{Y_{33}^E d_{33}^2}{\epsilon_3^T}$ [13]:

$$\delta_3=\Delta\sin(\kappa z)e^{j\omega t} \tag{5}$$

$$T_3=Y_{33}^D\kappa\Delta\left(\cos(\kappa z)-\cos(\kappa l)\right)e^{j\omega t} \tag{6}$$

$$E_3=\frac{\kappa\Delta}{d_{33}(1-k_{33}^2)}\left(-k_{33}^2\cos(\kappa z)+\cos(\kappa l)\right)e^{j\omega t} \tag{7}$$

These expressions provide means to analyze the PR's mechanical and electrical limits, which we utilize in Section V for calculating maximum power density. Inserting (5) back into (4) also reveals the radial frequency ω to be

$$\omega=\kappa\sqrt{\frac{Y_{33}^D}{\rho}} \tag{8}$$

Equations (5)-(8) enable derivation of an electrical model for the PR (ie. the Butterworth-Van Dyke model [15]) based on its impedance. This model is illustrated in Fig. 2 and has the following parameters for sinusoidal excitation of the PR's lowest resonant mode [13], [16]–[18]:

[1]Different measurement conditions for ϵ_3 and Y_{33} have the following relationships: $\epsilon_3^S=(1-k_{33}^2)\epsilon_3^T$; $Y_{33}^E=(1-k_{33}^2)Y_{33}^D$ [13].

$$C_p=\epsilon_3^S\frac{A}{l} \tag{9}$$

$$C=C_p\frac{8}{\pi^2}k_{33}^2=\frac{8Y_{33}^E d_{33}^2(1-k_{33}^2)}{\pi^2}\frac{A}{l} \tag{10}$$

$$L=\frac{\rho l^2}{2C_p k_{33}^2 Y_{33}^D}=\frac{\rho}{2Y_{33}^{E2}d_{33}^2}\frac{l^3}{A} \tag{11}$$

$$R=\frac{1}{Q_m}\sqrt{\frac{L}{-C_p||C}}=\frac{1}{Q_m}\frac{l\gamma_o}{4C_p k_{33}^2}\sqrt{\frac{\rho}{Y_{33}^D}}=\frac{1}{Q_m}\frac{\gamma_o}{4\epsilon_3^S k_{33}^2}\sqrt{\frac{\rho}{Y_{33}^D}}\frac{l^2}{A} \tag{12}$$

where

$$\gamma_o=\sqrt{\pi^2-8k_{33}^2} \tag{13}$$

This electrical model serves as the basis for how we conceptualize the PR's behavior, and its full derivation can be found in Appendix A. It can be shown from (50) that κ takes on the following range for the PR's inductive region, with boundaries at the resonant and anti-resonant frequencies:

$$\frac{\gamma_o}{2l}<\kappa<\frac{\pi}{2l} \tag{14}$$

Also notable is the additional -C_p term in the LCR branch of Fig. 2. This term arises due to interaction between the applied and induced electric fields, which are parallel along z for the thickness extensional vibration mode [13].

III. Amplitude of Resonance Model

We employ the circuit model of Section II to analyze the PR's behavior in a power converter. Assuming i_L is sinusoidal, its amplitude (I_L) provides insight into the PR's amplitude of mechanical resonance, which determines the PR's mechanical energy storage and loss [4], [19]. The PR's ideal amplitude of resonance can be calculated from the total magnitude of charge it must transfer during each resonant cycle (illustrated in Fig. 3), which depends on the converter's specific switching sequence and operating point. This charge transfer calculation considers both the "connected/zero stages" (ie. stages when the PR is connected to the source-load system) and "open stages" (stages when the PR is open-circuited and C_p charges/discharges through resonance) of the switching sequence, thereby providing a realistic representation of the PR's behavior as used in a converter.

To evaluate piezoelectric materials, we assume either of the highest-efficiency step-down switching sequences analyzed in [4], [19], which have the following I_L:

$$I_L=\frac{\pi}{2}fQ_{total}=\pi\left(\frac{P_{out}}{V_{in}}+fC_pV_{in}\right) \tag{15}$$

In accordance with the switching sequences proposed in [4], [19], this calculation assumes resonant "soft" charging/discharging of the PR's C_p, zero voltage switching (ZVS) of all switches, and all-positive instantaneous power transfer for high efficiency. Thus, this I_L equation models the PR's amplitude of resonance for "optimal" converter operation, which we assume throughout this work.

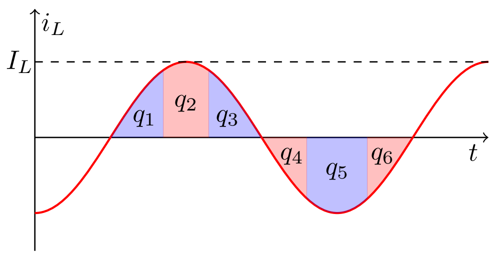

Fig. 3. Sinusoidal approximation of i_L (and resulting amplitude of resonance I_L) based on the charge transfer q_n required of each switching stage n. [4].

To model the PR's power transfer capability as a function of operating constraints, (15) can be rearranged such that power transfer is the following function of I_L:

$$P_{out} = \frac{1}{\pi} V_{in} I_L - C_p f V_{in}^2 = \frac{1}{\pi} V_{in} I_L - B V_{in}^2 \tag{16}$$

in which we have substituted

$$B = f C_p \tag{17}$$

Further, we can derive a model relating I_L to the PR's physical states using the coupled state equations in (1)-(3). The result establishes the following relationship between I_L and Δ (full derivation in Appendix B):

$$I_L = \frac{A}{l} \kappa \sqrt{\frac{Y_{33}^D}{\rho}} d_{33} Y_{33}^E \Delta \sin(\kappa l) \tag{18}$$

T_3 and E_3 can then be related to I_L through Δ, as determined by (6) and (7), respectively:

$$\Delta = \frac{1}{\kappa Y_{33}^D} \frac{1}{1 - \cos(\kappa l)} T_3 \tag{19}$$

$$\Delta = \frac{(1 - k_{33}^2)}{(\cos(\kappa l) - k_{33}^2)} \frac{d_{33}}{\kappa} E_3 \tag{20}$$

in which we have focused on $z = 0$, where T_3 and E_3 are maximum. Equations (16)-(20) establish a relationship between physical states and power transfer through I_L, which we utilize for deriving maximum power density in Section V.

IV. Minimum Loss Ratio and Associated Figure of Merit

To quantitatively compare piezoelectric materials for power conversion, we first focus on achievable PR efficiency; this has implications for both operating cost and thermal management. Efficiency can be expressed as

$$\eta = \frac{P_{out}}{P_{out} + P_{loss}} = \frac{1}{1 + \frac{P_{loss}}{P_{out}}} \tag{21}$$

Thus, the impact of piezoelectric material properties on efficiency can be examined through *loss ratio* P_{loss}/P_{out}, which is desired to be as low as possible. Material-dependent losses in the PR include mechanical loss and dielectric loss; for this FOM, we focus on mechanical loss.

To derive the minimum mechanical loss ratio for a piezoelectric material, we estimate mechanical loss using the PR's amplitude of resonance (15) and resistance as follows [4]:

$$P_{loss} = \frac{1}{2} I_L^2 R \tag{22}$$

P_{loss} can then be divided by P_{out} to produce the following mechanical loss ratio equation:

$$\frac{P_{loss}}{P_{out}} = \frac{\frac{1}{2} I_L^2 R}{P_{out}} = \frac{\pi^2}{2} \left(\frac{P_{out}}{V_{in}^2} R + 2BR + \frac{V_{in}^2 B^2}{P_{out}} R \right) \tag{23}$$

This loss ratio equation has only two operating point parameters (V_{in} and P_{out}) and two PR-dependent parameters (B and R). We can explicitly separate the PR's material and geometry properties by extracting A and l from B and R, leaving only the material-dependent B_o and R_o, respectively:

$$\frac{P_{loss}}{P_{out}} = \frac{\pi^2}{2} \left(\frac{P_{out}}{V_{in}^2} \frac{l^2}{A} R_o + 2 B_o R_o + \frac{V_{in}^2}{P_{out}} \frac{A}{l^2} B_o^2 R_o \right) \tag{24}$$

$$B_o = \frac{\epsilon_3^S}{2} \frac{\gamma_o}{\pi + \gamma_o} \sqrt{\frac{Y_{33}^D}{\rho}} \tag{25}$$

$$R_o = \frac{1}{Q_m} \frac{\gamma_o}{4 \epsilon_3^S k_{33}^2} \sqrt{\frac{\rho}{Y_{33}^D}} \tag{26}$$

in which we have assumed the resonant period to be the average[2] of the resonant and anti-resonant periods for the lowest resonant mode, which corresponds to a wave number of $\kappa = \frac{\gamma_o \pi}{(\gamma_o + \pi) l}$.

From here, we assume that the designer has the flexibility to choose the PR's geometric dimensions. The loss ratio equation reached in (24) is a second-order equation with respect to $\frac{A}{l^2}$, which implies the existence of a minimum (assuming all quantities are positive) as illustrated in Fig. 4(a). Taking the derivative of (24) with respect to $\frac{A}{l^2}$ and equating it to zero reveals the geometry condition for this minimum and the minimum mechanical loss ratio itself:

$$\frac{A}{l^2} = \frac{P_{out}}{V_{in}^2 B_o} \tag{27}$$

$$\Rightarrow \quad \left(\frac{P_{loss}}{P_{out}} \right)_{min} = 2\pi^2 B_o R_o = \frac{\pi^2 \gamma_o^2}{\pi + \gamma_o} \frac{1}{4 k_{33}^2 Q_m} \tag{28}$$

Thus, the PR's mechanical loss ratio can be minimized by strategically designing the PR's dimensions to satisfy (27) for its intended operating point. This condition cancels the operating point and PR geometry parameters in the loss ratio equation, so *the minimum mechanical loss ratio for a PR depends on only its material properties*. Taking the inverse of (28), the following unitless factor can therefore be considered a mechanical efficiency FOM (FOM_M) for piezoelectric materials whose value is desired to be as large as possible; its parameters are easily accessible in material datasheets.

$$\text{FOM}_M = 4 k_{33}^2 Q_m \frac{\pi + \gamma_o}{\pi^2 \gamma_o^2} \tag{29}$$

[2]At this average resonant period, the PR's charge transfer is split evenly between connected/zero stages and open stages as analyzed in [4], [19].

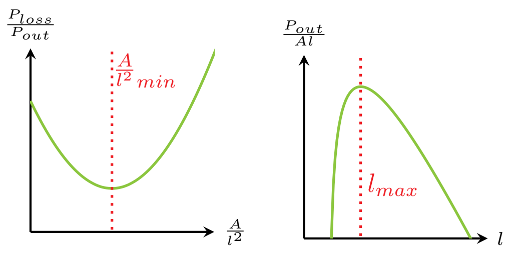

Fig. 4. On logarithmic axes, PR (a) loss ratio minimum and (b) volumetric power density maximum (the same concept applies to areal power density).

TABLE II
LOSS RATIO COMPARISON OF APC INTERNATIONAL PZT MATERIALS

Material	Q_m	k_{33}	PSSS [4]	Estimate (27)	% Error
840	500	0.72	.0102	.0102	0.26%
841	1400	0.68	.0041	.0041	0.96%
842	600	0.71*	.0086	.0086	0.44%
844	1500	0.65*	.0043	.0044	0.94%
850	80	0.72	.0660	.0624	5.8%
851	80	0.71*	.0689	.0649	6.0%
855	65	0.76	.0477	.0454	5.0%
880	1000	0.62	.0083	.0083	0.46%
881	1000	0.73*	.0047	.0047	0.80%

(*) Calculated using $k_{33}^2 = Y_{33}^E d_{33}^2/\epsilon_3^T$

We validate the minimum loss ratio in (28) and hence FOM in (29) with geometry and material data for 572 APC International discrete PR parts listed on [20]; these parts consist of round and rectangular plate-shaped PRs of varying dimensions, spanning nine total materials. For each part, we calculate its PR circuit model parameters and then solve for an exact periodic steady state solution (PSSS) of the PR's states as detailed in [4], assuming the converter switching sequence corresponding to (15) with V_{in}=100 V. Given these specifications, we then sweep P_{out} across multiple PSSSs for each part in order to identify its minimum loss ratio.

Ultimately, *all discrete parts of the same material yield the same minimum loss ratio*, validating the independence of (28) and (29) from operating point and PR geometry. In Table II, these PSSS-calculated minimum loss ratios are compared with the estimate of (28) and demonstrate less than 1% error for all low-loss-ratio materials (the error is higher for lossier materials because (15) does not account for additional charge transfer required to make up for loss). Thus, the minimum mechanical loss ratio in (28) and the mechanical efficiency FOM in (29) serve as representative metrics for comparing the efficiency capabilities of low-loss piezoelectric materials.

V. MAXIMUM POWER DENSITY AS A FIGURE OF MERIT

A second point of comparison for piezoelectric materials is achievable power handling density, which poses a boundary for converter miniaturization. A useful power density metric must consider how the PR is to be utilized in a converter (ie. not just energy density), so we again assume the amplitude of resonance model in Section III. Using (16), we derive maximum power density considering physical limits for I_L.

A. Maximum Amplitude of Resonance

The maximum permissible I_L depends on the PR's maximum amplitude of mechanical resonance, constrained by limits such as stress, electric field, or loss density. T_3 and E_3 are both functions of Δ, so their limits can each be related to I_L through Δ as described in Section III[3]. Thus, I_{Lmax} depends on δ_{omax} as follows:

$$I_{Lmax} = \frac{A}{l}\kappa Y_{33}^E d_{33}\delta_{omax}\sin(\kappa l)\sqrt{\frac{Y_{33}^D}{\rho}} \qquad (30)$$

This results in the following stress-limited (I_{LmaxT}) and electric-field-limited (I_{LmaxE}) maximum amplitudes of resonance:

$$I_{LmaxT} = \frac{A}{l}d_{33}(1-k_{33}^2)T_{max}\sqrt{\frac{Y_{33}^D}{\rho}}\frac{\sin(\kappa l)}{1-\cos(\kappa l)} \qquad (31)$$

$$I_{LmaxE} = \frac{A}{l}\epsilon_3^S k_{33}^2 E_{max}\sqrt{\frac{Y_{33}^D}{\rho}}\frac{\sin(\kappa l)}{\cos(\kappa l)-k_{33}^2} \qquad (32)$$

in which we suggest use of the wave number in Section IV ($\kappa = \frac{\gamma_o \pi}{l(\gamma_o+\pi)}$) for consistency between FOMs.

Since their geometry terms are identical, the relative magnitudes of I_{LmaxT} and I_{LmaxE} can be compared based on only their geometry-extracted quantities (ie. (31) and (32) without $\frac{A}{l}$); these are functions of only material properties, so we refer to them as I_{LmaxTo} and I_{LmaxEo}, respectively. The lower-magnitude limit then serves as the geometry-normalized maximum for I_L:

$$I_{Lmax} = \frac{A}{l}I_{Lmaxo} = \frac{A}{l}\min(I_{LmaxTo}, I_{LmaxEo}) \qquad (33)$$

Thus, (33) provides an expression for I_{Lmax} in terms of only material properties and geometry terms; this enables maximization of power density considering material limits in Sections V-B and V-C.

B. Volumetric Power Density

Volumetric power density can be derived from the amplitude of resonance model described in Section III. Dividing (16) by volume yields:

$$\frac{P_{out}}{Al} = \frac{1}{\pi Al}V_{in}I_L - \frac{1}{Al}BV_{in}^2 \qquad (34)$$

We can then set I_L equal to I_{Lmax} in (33) and separate geometry terms from material properties to arrive at:

$$\frac{P_{out}}{Al} = \frac{1}{\pi l^2}V_{in}I_{Lmaxo} - \frac{1}{l^3}B_oV_{in}^2 \qquad (35)$$

This power density expression can be maximized by again assuming that the designer has the flexibility to choose l. Taking the derivative of (34) with respect to l and equating it to zero results in the following l condition and maximum power density as illustrated in Fig. 4(b):

$$l_{max} = \frac{3\pi}{2}\frac{B_oV_{in}}{I_{Lmaxo}} \qquad (36)$$

[3]It should be noted that V_{in} in (16) is purely the input voltage and does not have a fixed relationship to $v_{p,1}$ (the first harmonic of v_p) in (47). Thus, V_{in} cannot be directly affixed to physical limits like T_{max} and E_{max}.

$$\Rightarrow \quad \left(\frac{P_{out}}{Al}\right)_{max} = \frac{4}{27\pi^3}\frac{I_{Lmaxo}^3}{B_o^2 V_{in}} \tag{37}$$

Thus, maximum power density depends on only material properties and the inverse of V_{in}, which permits direct comparison between materials using only material data. The translates to the following volumetric power density FOM (FOM_{VPD}):

$$\text{FOM}_{VPD} = \frac{4}{27\pi^3}\frac{I_{Lmaxo}^3}{B_o^2} \tag{38}$$

which has units V·W/m^3.

C. Areal Power Density

In some applications, power handling capability for a given footprint area may be more useful to the designer than volumetric power density. This metric also becomes more relevant for highly-planar PR designs, as often dictated by (27). Similar to (34), the areal power density can be written as follows with $I_L = I_{Lmax}$ and geometry terms extracted:

$$\frac{P_{out}}{A} = \frac{1}{\pi l}V_{in}I_{Lmaxo} - \frac{1}{l^2}B_o V_{in}^2 \tag{39}$$

This expression can likewise be maximized by equating its derivative with respect to l to zero, resulting in the following l condition and maximum footprint power density:

$$l_{max} = \frac{2\pi B_o V_{in}}{I_{Lmaxo}} \tag{40}$$

$$\Rightarrow \quad \left(\frac{P_{out}}{A}\right)_{max} = \frac{I_{Lmaxo}^2}{4\pi^2 B_o} \tag{41}$$

Like the minimum loss ratio in (28), all operating point and geometry terms cancel in (41) for the condition specified in (40). Thus, *the maximum areal power density for a PR depends on only its material properties*. (41) therefore serves as a FOM in itself, permitting direct comparison of footprint requirements between piezoelectric materials.

$$FOM_{APD} = \frac{I_{Lmaxo}^2}{4\pi^2 B_o} \tag{42}$$

with units W/m^2.

VI. Loss Density Considerations

While the maximum PR power densities derived in Section V consider physical material limits such as stress and electric field, they do not consider the thermal implications of loss. Realistically, thermal management limitations may confine power density to significantly lower boundaries than the material's physical limits. We treat this subject by analyzing loss density.

For the solidly-mounted PR in Fig. 1(a), we assume that most heat extraction occurs through the fixed electrode surface at $z = 0$, which has area A. We further assume that a maximum quantity of PR loss per A can be accommodated by a given thermal design such that the PR's temperature rise remains permissible. This maximum areal loss density relates to the PR's operation as follows, considering only mechanical losses:

$$\frac{P_{loss}}{A} = \frac{1}{2}\frac{I_L^2 R}{A} = \frac{1}{2}I_{Lo}^2 R_o \tag{43}$$

in which we have extracted geometry parameters from I_L ($I_L = \frac{A}{l}I_{Lo}$) and R.

(43) reveals a direct relationship between maximum areal loss density and the PR's states through I_{Lo}, without dependence on geometry or operating point parameters. This loss density equation can be utilized to calculate the expected loss density for a given I_{Lo} and material. Conversely, it can be rearranged to define a loss-limited maximum for I_L:

$$I_{LmaxL} = \frac{A}{l}\sqrt{\frac{2}{R_o}\left(\frac{P_{loss}}{A}\right)_{max}} \tag{44}$$

Because $I_{LmaxL} \propto \frac{A}{l}$, it can be seamlessly compared to I_{LmaxT} and I_{LmaxE} in (33) and/or inserted into (37) or (41) to calculate maximum power density given a maximum loss density. Although practically useful, this comparison or power density calculation relies on both thermal transfer and material properties, as I_{LmaxL} requires an assumption for $\left(\frac{P_{loss}}{A}\right)_{max}$.

VII. Material Comparison

Equipped with FOMs for mechanical efficiency and power density, we now evaluate commercially-available variants of PZT (the most widely-utilized piezoelectric material) for use in power conversion. This study is confined to "hard" PZT materials, which tend to have both greater physical limits and higher quality factors than "soft" materials. We collect the following properties for hard PZT materials from eight different manufacturers: Q_m, ϵ_3^T, Y_{33}^E, d_{33}, ρ, and maximum voltage or electric field (if provided). k_{33} is calculated using $k_{33}^2 = \frac{Y_{33}^E d_{33}^2}{\epsilon_3^T}$, and sinusoidal amplitude E_{max} is conservatively assumed to be half the reported electric field limit[4]. Materials without a reported electric field limit are assumed to have the same maximum as similar materials from the same manufacturer or a limit of 1 kV/mm (a common value among most manufacturers). Due to sparse reporting of material-specific limits, this maximum electric field is assumed to correlate with material's true electrical or mechanical limit.

We then use these properties to calculate the mechanical and power density FOMs for each of 51 total materials. Fig. 5 displays these results with one FOM on each axis, overlaid with loss-density contour lines to visualize thermal management needs. Materials with manufacturer-provided limits for electric field have solid-filled markers, while materials with assumed electric field limits are differentiated by unfilled markers. The considered materials exhibit wide variation in terms of both mechanical efficiency and power density capabilities.

Fig. 5 is constructed such that assumptions for maximum loss density are left to the reader (as they will vary based on design and application constraints). For a given areal loss density limit, all points above the corresponding contour line should be projected downward (in the -y direction, keeping constant FOM_M) onto the allowable heat transfer line itself; this new point conveys their maximum power densities given

[4]At the anti-resonant frequency, for example, v_p resembles a sinusoid with dc offset $V_{in}/2$ and amplitude $V_{in}/2$. Thus, the sinusoidal amplitude is half the true maximum value of $v_p = V_{in}$.

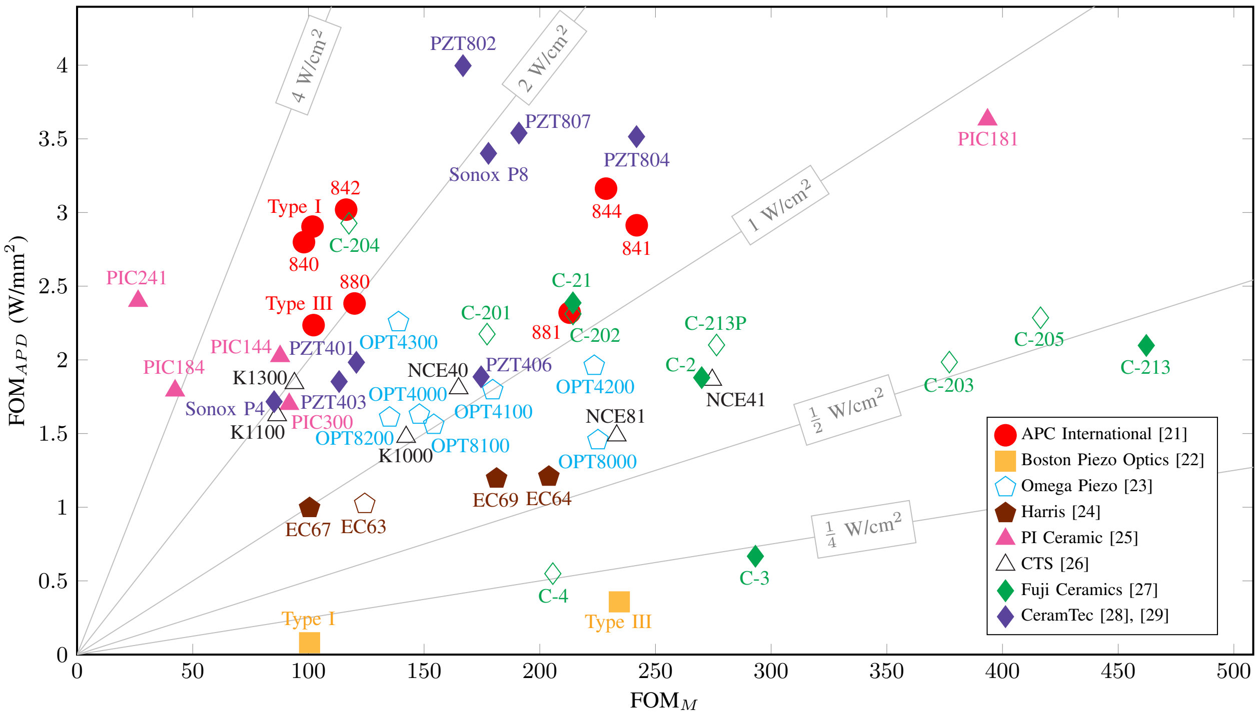

Fig. 5. Comparison of hard PZT materials for power conversion based on FOM$_M$ and FOM$_{APD}$, overlaid with areal-loss-density contour lines. Filled and unfilled markers indicate manufacturer-provided and author-estimated electric field limits, respectively.

the assumed limit. Thus, it can be inferred that many materials would never reach their electric field limits without aggressive thermal designs; for a given heat transfer capability, higher power density is instead enabled by a higher FOM_M.

In addition to PZT, there are numerous other piezoelectric material types that may be similarly compared for power conversion using these FOMs. For this study, it should be noted that (1) dielectric loss has not been considered, (2) the k_{33} electromechanical coupling coefficient has been assumed (as PR designs become more planar, the k_t coefficient becomes more representative than k_{33}), and (3) the results of Fig. 5 are sensitive to variation between manufacturers in terms of measurement procedure and/or reporting of physical limits.

VIII. Application to Design

In addition to material metrics, these FOM derivations provide PR geometry design guidance for maximum efficiency and maximum power density. The conditions for maximum power density in Section V constrain only l, while the condition for minimum loss ratio in Section IV defines a relationship between A and l. Thus, both the maximum power density and the minimum loss ratio for a nominal operating point can be achieved in a PR design by strategically selecting l from (36) or (40) and then A to satisfy (27) as visualized in Fig. 4.

We demonstrate an example PR design based on these geometry criteria with the PIC181 material; Fig. 5 shows PIC181 to be capable of the highest power density given a loss density limit of 1 W/cm^2. For an example operating point with V_{in} = 100 V, V_{out} = 60 V, and P_{out} = 10 W, l and A are calculated from (40) and (27) to be 0.11 mm and 2.75 mm^2, respectively, assuming E_{max} = 750 V/mm. The corresponding PR model parameters from (9)-(12) are shown in Fig. 6. We calculate an exact PSSS for this PR as utilized in the topology of Fig. 6 with the V_{in}-V_{out}, *Zero*, V_{out} switching sequence [4]; this is a high-efficiency operating mode that corresponds directly to the amplitude of resonance model of Section III. The PSSS switching times are then used to simulate this operating point in LTspice, producing the expected switching sequence waveforms shown in Fig. 7.

LTspice-calculated operating point information for this simulation is compared in Table III with the intended figures. It is shown that the exact minimum loss ratio is achieved, corresponding to a PR efficiency of 99.75% and an areal loss density of 0.92 W/cm^2. E_{max} is calculated using (32) with the simulated values for I_L and f (for κ) and likewise demonstrates the design value. Thus, the derived FOMs are validated, and both maximum efficiency and maximum power density can be achieved with intentional PR geometry design[5] using the provided conditions. Although this simulated design is ideal in nature (ie. it has ideal switches, assumes k_{33} instead of k_t, assumes ideal PR mounting, and only considers mechanical loss), it illustrates auspicious potential for power conversion based on piezoelectrics.

[5]Designers employing these geometry guidelines should be reminded that: (1) The specific amplitude of resonance model presented in Section III directly applies to only the highest-efficiency switching sequences of [4] for the $2V_{out} > V_{in} > V_{out}$ operating region (models serving other operating regions are also provided in [4]). Thus, the derived minimum loss ratio and maximum power density quantities should be considered only as relative material comparison metrics outside of this region. (2) The minimum loss ratio is achievable only when the condition (27) is met; surrounding operating points will have higher loss ratios. The same concept applies to maximum power density, which decreases for the same limits as the operating point deviates from (36) or (40).

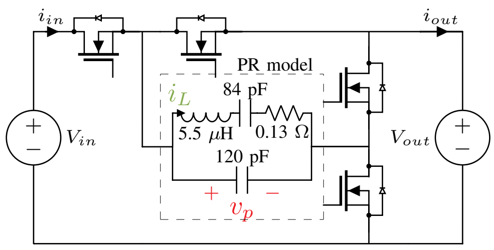

Fig. 6. Converter topology as simulated in LTspice.

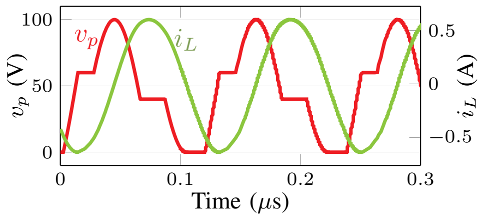

Fig. 7. LTspice-simulated time-domain waveforms for switching sequence V_{in}-V_{out}, *Zero*, V_{out} with V_{in} = 100 V, V_{out} = 60 V, and P_{out} = 10 W [19].

TABLE III
DESIGN OPERATING POINT

Value	Calculation	Simulation
P_{out}	10 W	10.02 W
$\frac{P_{loss}}{P_{out}}$	0.25%	0.25%
f	8.38 MHz	8.48 MHz
I_L	628 mA	601 mA
E_{max}	750 V/mm	750 V/mm
$\frac{P_{out}}{A}$	3.6 W/mm^2	

IX. Power Handling Scaling Properties

Piezoelectric energy storage has been suggested to have advantageous power density and efficiency scaling properties compared to magnetics [3]. With an example design illustrated in Section VIII, we now analyze specifically how PR power handling properties scale with size in the realistic converter implementation depicted by the amplitude of resonance model. (16) can be re-written as:

$$P_{out} = A\left(\frac{1}{\pi l}V_{in}I_{Lo} - \frac{1}{l^2}B_o V_{in}^2\right) \tag{45}$$

in which we have assumed a fixed I_{Lo} limit (and therefore fixed stress/electric-field limits) as derived in Section V. This expression shows that P_{out} scales linearly with A, but the expression contained in parenthesis has a global maximum at $l = \frac{2\pi V_{in} B_o}{I_{Lo}}$ such that

$$(P_{out})_{max} = A\frac{I_{Lo}^2}{4\pi^2 B_o} \tag{46}$$

Thus, maximum power handling scales with only A and material properties for a fixed I_{Lo}.

From here, we postulate scaling the PR in all three dimensions by scaling factor α as conducted for magnetics in [1]. In the case of a PR, volume scales by α^3, but (46) suggests that the maximum power handling would scale by α^2 assuming a fixed I_{Lo}. This implies that maximum volumetric power density scales inversely with α (which confers with (37), assuming the direct relationship between V_{in} and l_{max} in (36)), and that maximum power area-density in (41) remains constant. In terms of loss, both the minimum loss ratio in (28) and the areal loss density for a given I_{Lo} in (43) have no geometry dependence and therefore remain fixed regardless of α. The required operating frequency scales with α^{-1}, however, which may impose a practical scaling limit.

These geometry dependencies and scaling properties for piezoelectrics are summarized in Table IV. As volume is scaled downward ($\alpha < 1$), maximum volumetric power density increases while minimum loss ratio (and therefore maximum efficiency) stays constant. These are favorable scaling properties for converter miniaturization.

X. Conclusion

To evaluate piezoelectric materials for power conversion, we have derived figures of merit for achievable efficiency and power density based on realistic converter operation. These figures of merit depend on only material properties (and - if

TABLE IV
POWER HANDLING SCALING PROPERTIES OF PIEZOELECTRICS

Property	PR Geometry Dependence	PR Scaling (fixed $\frac{P_{loss}}{A}$)
$(P_{out})_{max}$	A	α^2
$(\frac{P_{out}}{vol})_{max}$	l^{-1}	α^{-1}
$(\frac{P_{loss}}{P_{out}})_{min}$	none	constant
$\frac{P_{loss}}{vol}$	l^{-1}	α^{-1}

considered - assumptions of heat transfer limits), and we have employed them to compare the capabilities of 51 PZT-based materials. Although these materials exhibit wide variability with respect to the FOMs, those with higher efficiency figures of merit are capable of achieving the highest power densities for realistic loss density limits.

In addition to material metrics, these derivations reveal PR geometry design guidelines for realizing both maximum efficiency and power density. We have illustrated an example PR design using these criteria, which has been validated along with the derived figures of merit in LTSpice simulations. The simulated design attests to highly promising efficiency and power density capabilities for piezoelectrics, and fundamental derivations show that these properties scale favorably for converter miniaturization.

Acknowledgment

The authors gratefully acknowledge Yinglai Xia and Jeronimo Segovia-Fernandez with Texas Instruments for insightful discussions pertaining to this work.

Appendix A
Electrical Model Derivation

The electrical model of Fig. 2 can be derived from the PR's impedance characteristic surrounding its lowest thickness extensional resonant mode. First, $v_{p,1}$ (the first harmonic of v_p) and i_{in} can be derived from (2), (6), and (7) to be

$$v_{p,1} = -\int_0^l E dz = \frac{\kappa \Delta l}{d_{33}(1-k_{33}^2)}\left(\frac{k_{33}^2}{\kappa l}\sin(\kappa l) - \cos(\kappa l)\right)e^{j\omega t} \tag{47}$$

$$i_{in} = -j\omega D A = -j\omega A\frac{\kappa \Delta \epsilon_3^T}{d_{33}}\cos(\kappa l)e^{j\omega t} \tag{48}$$

which constitute the following impedance for an ideal PR:

$$Z = \frac{v_{p,1}}{i_{in}} = \frac{l}{j\omega\epsilon_3^S A}\left(1 - \frac{k_{33}^2}{\kappa l}\tan(\kappa l)\right) \tag{49}$$

Approximating the tangent term in (49) with the first term of the power series expansion described in [13] yields:

$$Z = \frac{v_{p,1}}{i_{in}} = \frac{l}{j\omega\epsilon_3^S A}\left(1 - \frac{8k_{33}^2}{\pi^2 - 4\kappa^2 l^2}\right) \tag{50}$$

Similarly, the circuit model of Fig. 2 has the following impedance for an ideal PR ($R = 0$):

$$Z = \frac{1}{j\omega C_p}\left(\frac{C_p - C - \omega^2 LCC_p}{C_p - \omega^2 LCC_p}\right) \tag{51}$$

Setting (50) equal to (51) and solving for C_p, C, and L yields the circuit model parameters in equations (9)-(11).

Appendix B
IL Relationship to PR States Derivation

The relationship between I_L and the PR's physical states can be derived using the coupled state equations in (1)-(3) and our solution in (5)-(7). Inserting (1) into (2) yields:

$$D_3 = d_{33}Y_{33}^E \frac{\partial \delta_3}{\partial z} + \left(\epsilon_3^T - d_{33}^2 Y_{33}^E\right) E_3 \tag{52}$$

Multiplying by area and integrating with respect to z across the length of the PR (from $z = 0$ to $z = l$) gives:

$$Q_3 = \frac{A}{l} d_{33}Y_{33}^E \delta_3(l) - \frac{A}{l}\left(\epsilon_3^T - d_{33}^2 Y_{33}^E\right) v_{p,1} \tag{53}$$

Finally, taking the time derivative and inverting for the desired sign convention of Fig. 2 yields:

$$i_{in} = C_p \frac{dv_{p,1}}{dt} - \frac{A}{l} j\omega d_{33} Y_{33}^E \delta_3(l) \tag{54}$$

which corresponds to the model of Fig. 2 such that

$$I_L = \frac{A}{l}\kappa\sqrt{\frac{Y_{33}^D}{\rho}} d_{33}Y_{33}^E \Delta \sin(\kappa l) \tag{55}$$

in which we have inserted (8) for ω.

References

[1] C. R. Sullivan, B. A. Reese, A. L. Stein, and P. A. Kyaw, "On size and magnetics: Why small efficient power inductors are rare," in *Proc. IEEE Intl. Symposium on 3D Power Electronics Integration and Manufacturing*, Raleigh, NC, USA, Jun. 2016, pp. 1–23.

[2] D. J. Perreault, J. Hu, J. M. Rivas, Y. Han, O. Leitermann, R. C. Pilawa-Podgurski, A. Sagneri, and C. R. Sullivan, "Opportunities and challenges in very high frequency power conversion," in *Proc. IEEE Applied Power Electronics Conference and Exposition*, Washington, DC, USA, Feb. 2009, pp. 1–14.

[3] P. A. Kyaw, A. L. Stein, and C. R. Sullivan, "Fundamental examination of multiple potential passive component technologies for future power electronics," *IEEE Transactions on Power Electronics*, vol. 33, no. 12, pp. 10,708–10,722, 2018.

[4] J. D. Boles, J. J. Piel, and D. J. Perreault, "Enumeration and analysis of dc-dc converter implementations based on piezoelectric resonators," *IEEE Transactions on Power Electronics*, vol. 36, no. 1, pp. 129–145, 2021.

[5] W. Braun, Z. Tong, and J. Rivas-Davila, "Inductorless soft switching dc-dc converter with an optimized piezoelectric resonator," in *Proc. IEEE Applied Power Electronics Conference and Exposition*, New Orleans, LA, USA, Mar. 2020, pp. 2272–2278.

[6] S. Moon and J.-H. Park, "High power dc–dc conversion applications of disk-type radial mode Pb (Zr, Ti) O3 ceramic transducer," *Japanese Journal of Applied Physics*, vol. 50, no. 9S2, p. 09ND20, 2011.

[7] B. Pollet, G. Despesse, and F. Costa, "A new non-isolated low power inductorless piezoelectric dc-dc converter," *IEEE Transactions on Power Electronics*, vol. 34, no. 11, pp. 11 002–11 013, 2019.

[8] A. M. Flynn and S. R. Sanders, "Fundamental limits on energy transfer and circuit considerations for piezoelectric transformers," *IEEE Transactions on Power Electronics*, vol. 17, no. 1, pp. 8–14, 2002.

[9] J. M. Alonso, C. Ordiz, and M. A. Dalla Costa, "A novel control method for piezoelectric-transformer based power supplies assuring zero-voltage-switching operation," *IEEE Transactions on Industrial Electronics*, vol. 55, no. 3, pp. 1085–1089, 2008.

[10] M. Ekhtiari, T. Andersen, M. A. Andersen, and Z. Zhang, "Dynamic optimum dead time in piezoelectric transformer-based switch-mode power supplies," *IEEE Transactions on Power Electronics*, vol. 32, no. 1, pp. 783–793, 2017.

[11] E. L. Horsley, A. V. Carazo, N. Nguyen-Quang, M. P. Foster, and D. A. Stone, "Analysis of inductorless zero-voltage-switching piezoelectric transformer-based converters," *IEEE Transactions on Power Electronics*, vol. 27, no. 5, pp. 2471–2483, 2012.

[12] J. D. Boles, E. Ng, J. H. Lang, and D. J. Perreault, "High-efficiency operating modes for isolated piezoelectric-transformer-based dc-dc converters," in *Proc. IEEE Workshop on Control and Modeling for Power Electronics*, Aalborg, Denmark, Nov. 2020, pp. 1–8.

[13] J. Erhart, P. Půlpán, and M. Pustka, *Piezoelectric Ceramic Resonators*. Springer, 2017.

[14] H. H. Woodson and J. R. Melcher, *Electromechanical Dynamics Part III: Elastic and Fluid Media*. Wiley, 1968.

[15] K. S. Van Dyke, "The piezo-electric resonator and its equivalent network," *Proceedings of the Institute of Radio Engineers*, vol. 16, no. 6, pp. 742–764, 1928.

[16] A. Ballato, "Modeling piezoelectric and piezomagnetic devices and structures via equivalent networks," *IEEE Transactions on Ultrasonics, Ferroelectrics, and Frequency Control*, vol. 48, no. 5, pp. 1189–1240, 2001.

[17] S. Sherrit, S. P. Leary, B. P. Dolgin, and Y. Bar-Cohen, "Comparison of the Mason and KLM equivalent circuits for piezoelectric resonators in the thickness mode," in *Proc. IEEE Ultrasonics International Symposium*, vol. 2, Tahoe, NV, USA, Oct. 1999, pp. 921–926.

[18] L. Wang and R. P. Burgos, "Comprehensive analysis of models and operational characteristics of piezoelectric transformers," in *Proc. IEEE Applied Power Electronics Conference and Exposition*, New Orleans, LA, USA, Mar. 2020, pp. 1422–1429.

[19] J. D. Boles, J. J. Piel, and D. J. Perreault, "Analysis of high-efficiency operating modes for piezoelectric resonator-based dc-dc converters," in *Proc. IEEE Applied Power Electronics Conference and Exposition*, New Orleans, LA, USA, Mar. 2020, pp. 1–8.

[20] "Ready to deliver piezoelectric ceramics". APC International. [Online]. Available: https://www.americanpiezo.com/piezo-sale/piezoelectric-ceramics.html

[21] "Physical and piezoelectric properties of APC materials". APC International, Ltd. [Online]. Available: https://www.americanpiezo.com/apc-materials/physical-piezoelectric-properties.html

[22] "Ceramic materials". Boston Piezo Optics Inc. [Online]. Available: https://www.bostonpiezooptics.com/ceramic-materials-pzt

[23] "Ceramic components". Omega Piezo Technologies. [Online]. Available: https://www.omegapiezo.com/ceramic-components/

[24] "Electro-ceramic products and material specifications". Harris Corporation. [Online]. Available: https://www.harris.com/sites/default/files/downloads/solutions/harris-electro-ceramic-products-and-material-specification-es.pdf

[25] "Material data". PI Ceramic GmbH. [Online]. Available: https://static.piceramic.com/fileadmin/user_upload/physik_instrumente/files/datasheets/PI_Ceramic_Material_Data.pdf

[26] "PZT materials complete properties". CTS Corporation. [Online]. Available: https://www.ctscorp.com/wp-content/uploads/CTS_-PZT-Materials_Complete-Properties_20180829.pdf

[27] "Piezo ceramics". Fuji Ceramics Corporation. [Online]. Available: http://www.fujicera.co.jp/managed/wp-content/themes/fujicera/digitalbook/en/elements/index_h5.html#1

[28] "Piezoceramic hard materials material data". CeramTec. [Online]. Available: https://www.ceramtec.com/files/ms_piezoceramic-hard-materials_en_de.pdf

[29] D. Berlincourt, H. Krueger, and C. Near, "Properties of Morgan electro ceramic ceramics," *Technical Publication TP-226, Morgan Electro Ceramics*, 2000.